1

2

3

Supraorbital whiskers act as wind-antennae in rat anemotaxis

6

7

8

Matias Mugnaini[1,2*], Dhruv Mehrotra[1,3,4*], Federico Davoine[1,5*], Varun Sharma[1,6*], Ana Rita Mendes[1,7*], Ben Gerhardt[8], Miguel Concha-Miranda[8], Michael Brecht[1,8‡] & Ann M. Clemens[1,9‡]

* contributed equally
‡ shared senior authorship
[1] Neural Systems & Behavior, Marine Biological Laboratory, 7 MBL Street, Woods Hole, MA 02543 USA
[2] Laboratory of Physiology and Algorithms of the Brain, Leloir Institute (IIBBA-CONICET), Av. Patricias Argentinas 435, Buenos Aires, Argentina.
[3] Integrated Program in Neuroscience, McGill University, 845 Sherbrooke St W, Montreal, QC, Canada
[4] Montreal Neurological Institute and Hospital, McGill University, Montreal, QC, Canada
[5] Instituto de Ingeniería Eléctrica, Facultad de Ingeniería, Universidad de la República, 3RJM+898, Montevideo, Uruguay
[6] School of Biological Sciences & Graduate Program in Quantitative Biosciences, Georgia Institute of Technology, North Ave NW, Atlanta, GA, 30332 USA
[7] Champalimaud Neuroscience Programme; Champalimaud Foundation, Av. Brasília, Doca de Pedrouços, 1400-038 Lisbon, Portugal
[8] Bernstein Center for Computational Neuroscience, Humboldt University of Berlin, Philippstr. 13 Haus 6, 10115 Berlin, Germany
[9] University of Edinburgh, Simons Initiative for the Developing Brain, 1 George Square, EH8 9JZ, Edinburgh, Scotland, United Kingdom

Corresponding authors: MB & AC

Running Title: Wind whiskers
Keywords: barrel cortex, anemotaxis, whisker, supra-orbital vibrissa, biomechanics, micro-CT, neuropixels

41

Abstract

43

We know little about mammalian anemotaxis, wind-sensing. Recently, however, Hartmann and colleagues showed whisker-based anemotaxis in rats. To investigate how whiskers sense airflow, we tracked whisker tips in anesthetized or cadaver rats under no airflow, low airflow and high (fan-blowing) airflow. Whisker tips showed little movement under no airflow conditions and all whisker tips moved during high airflow. Low airflow conditions – most similar to naturally occurring wind stimuli – engaged whisker tips differentially. Most whiskers moved little, the long supraorbital whisker showed maximal displacement and α, A1, β, and γ whiskers also showed movements. The long supraorbital whisker differs from other whiskers in its exposed dorsal position, upward bending, length and thin diameter. *Ex vivo* extracted long supraorbital whiskers also showed exceptional airflow displacement, suggesting whisker-intrinsic biomechanics mediate the unique airflow-sensitivity. Micro computed tomography revealed that the ring-wulst – the follicle structure receiving the most sensitive afferents – was more complete/ closed in supraorbital and other wind-sensitive whiskers than in non-wind-sensitive whiskers, suggesting specialization of the supraorbital for omni-directional sensing. We localized and targeted the cortical supraorbital whisker representation in simultaneous Neuropixels recordings with D/E-row whisker barrels. Responses to wind-stimuli were stronger in the supraorbital whisker representation than in D/E-row barrel cortex. We assessed the behavioral significance of whiskers in an airflow-sensing paradigm. We observed that rats spontaneously turn towards airflow stimuli in complete darkness. Selective trimming of wind-responsive whiskers diminished airflow turning responses more than trimming of non-wind-responsive whiskers. Lidocaine injections targeted to supraorbital whisker follicles also diminished airflow turning responses compared to control injections. We conclude that supraorbital whiskers act as wind antennae.

71

New and Noteworthy

73

Animals rely on sensory processing of airflow (anemotaxis) to guide navigation and survival. We examined mechanisms of rat anemotaxis by combining whisker tracking, biomechanical analysis, micro computed tomography of follicle structure, Neuropixels recordings in the barrel field, behavior of airflow turning and whisker interference by trimming and lidocaine injections. This diversity of methods led to a coherent pattern of results. Whiskers greatly differ in their airflow sensitivity and strongly wind-responsive whiskers – in particular long supraorbital whiskers – determine behavioral responses to airflow stimuli in rats.

82

83 **Introduction**

84 Animals can react to airflow stimuli and such wind-sensing abilities are referred to as
85 anemotaxis. The best studied examples of such behaviors come from insects, where
86 anemotactic turning has been studied amongst other species in crickets (Tauber &
87 Camhi 1995; Landolfa & Miller 1995) and in *Drosophila* (Kalmus 1942; Jovanic et al
88 2019). Crickets show fast (Tauber & Camhi 1995), highly sensitive (Landolfa & Miller
89 1995) and directional escape responses to airflow stimuli. In *Drosophila*, the antennae
90 are important transducers of anemotactic reactions (Suver et al. 2019). Until recently,
91 little was known about the anemotactic abilities of mammals, but Hartmann and
92 colleagues showed in 2016 (Yu et al 2016) in a conditioning paradigm that rats can
93 sense airflow. Deficits in airflow sensing after trimming of all whiskers then suggested
94 that this form of airflow sensing is whisker-mediated. The same authors also
95 characterized airflow mechanical responses of mystacial whiskers (Yu, Graff &
96 Hartmann 2016) and responses of rat trigeminal ganglion cells to air flow stimuli (Yan,
97 Bush & Hartmann 2019).

98 Our work was inspired by the whisker-anemotaxis shown by Hartmann & colleagues.
99 Rather than focus on the five rows of mystacial whiskers, which are represented in the
100 famous posteromedial-barrel-subfield (Woolsey & Van der Loos 1970), we decided to
101 assess the role of all facial whiskers in anemotaxis. The decision to look across different
102 whisker subfields was based on our experience that whisker subfields may have very
103 different functional characteristics. The submandibular whisker trident, for example
104 (The et al 2013), is a three-whisker-array involved in ground sensing. These whiskers
105 appear to possess biomechanical specializations for ground sensing and may provide
106 the animal with ego-motion-information about speed and heading direction (The et al.
107 2013, Chorev et al. 2016). While the mystacial macrovibrissae have been studied in
108 detail, we know little about the other ~300 whiskers on a rat (Brecht 2007). These
109 whiskers are organized in arrays (the upper and lower lip microvibrissae, the paw
110 whiskers, etc.). The few studies on microvibissae immediately suggested functional
111 differences between macro- and microvibrissae at the behavioral level (Brecht et al.
112 1997; Anjum et al. 2006) and the level of cortical representation (Elston, Pow and
113 Calford 1997).

114 The so-called supraorbital whiskers above the eye are of obvious interest in wind
115 sensing due to their exposed anatomical positioning. Understanding of whisker function
116 comes from understanding how whiskers interact in the environment (Grant et al. 2009,
117 Jadhav and Feldman 2010). Our analysis of whisker diversity in wind sensing took
118 advantage of recent progress in automated animal tracking, specifically of the
119 DeepLabCut toolbox (Mathis et al. 2018; Mathis & Mathis 2020). We asked the
120 following questions: (i) Which whiskers react maximally to airflow stimuli? (ii) Are
121 whisker airflow responses dependent on whisker biomechanics and sub-structure? (iii)
122 How do mechanical whisker airflow responses relate to the cortical barrel map? (iv)
123 How do whiskers contribute differentially to airflow sensitivity?

124 We find that whiskers differ markedly in their airflow responses. In particular, the
125 supraorbital whiskers respond distinctly when weak airflow stimuli are applied, such
126 airflow responses reflect the specific whisker biomechanics of the supraorbital

127   whiskers. Micro computed tomography (micro-CT) revealed follicular differences in

128   supra-orbital and pad whiskers. Recordings with Neuropixels probes show increased

129   wind response in the supraorbital vs pad barrel field. Finally, rats can sense and localize

130   weak airflow stimuli and such abilities are diminished by selective whisker trimming

131   of wind sensitive whiskers or by blocking supraorbital whiskers.

132

133

134

135

136

137

138

139

140

141 **Materials and methods**

142

143 All experiments complied with regulations on animal welfare and were approved
144 according to German law for animal welfare and approved by the State Office for
145 Health and Social Affairs committee (LAGeSo) in Berlin (Animal license number:
146 G0095-21 / 1.2) and Woods Hole, USA (21-10C and 22-09E).

147

148 *Whisker displacement*
149 Passive whisker movements were recorded in five rats (P19–P25), and a total of six
150 videos were analyzed. Acquisition was performed with a Logitech BRIO, ultra-HD
151 webcam at 60 frames per second (fps) (Logitech) under low-light conditions with fiber
152 optic illumination of the facial whiskers. Airflow was directed towards the face and
153 flow rate was controlled (passive flow and two variable fan speeds). Video tracking
154 was performed using DeepLabCut (Mathis et al 2018).

155

156 *Micro-CT imaging*
157 Whisker pads *acquired* from 7 male rats (P21—35) were scanned (five to six follicles
158 per whisker type were obtained). To achieve X-ray visibility of soft tissues, whole
159 whisker pads were stained in 1% Lugol's solution for 96 h or 1% phosphotungstic acid
160 (PTA) for 7 days and single vibrissa follicles in 1% Lugol's solution for 48 h, followed
161 by washing in 0.1 M phosphate buffer (PB) for 1 – 4 h (Metscher, 2009). For fixation
162 during scanning, samples were embedded in 2 – 4 % agarose and placed in a falcon
163 tube (whisker pads) or a 1 µl pipette tip (single vibrissa follicle). Micro-CT scans were
164 performed over a 360° rotation and pictures acquired every 0.2°, with exposure times
165 between 1 – 2 s, with 40 – 60 kV and 70 – 100 µA with an YXLON FF20 CT system
166 (YXLON International GmbH, Hamburg Germany) equipped with a Perkin Elmer Y
167 Panel 4343 CT detector and 190 kV nano focus transmission tube. Helical scans
168 allowed an effectively extended field of view in case of the whole whisker pad scans.

169

170 *Holotomography reconstructions*
171 Micro-CT scans were reconstructed with the YXLON reconstruction software. Images
172 were manually segmented in an extended version of the Amira software
173 (AmiraZIBEdition 2022.17, Zuse Institute Berlin, Germany) and exported labels
174 visualized with Dragonfly software (Dragonfly 2021.3, Object Research Systems
175 (ORS) Inc, Montreal, Canada). Adobe Illustrator (Version 26.3.1) was used for the
176 orientation and presentation of the data.

177

178 *Whisker morphology*
179 Three to four whiskers per whisker type from 6 rats (P19-P25; male=4, female =2; this
180 number includes the 4 male rats used in the Micro-CT scans) were plucked to measure
181 the whiskers length and diameter. Representative whisker images from Fig 2 were taken
182 either with an upright epifluorescence Zeiss microscope (Zen software, blue edition)
183 with brightfield (5X objective, Zeiss) (Fig 2B, top panel) or using an AVT Pike f421b

184　camera with a 60mm Nikon macro lens (Measurement and Automation Explorer,
185　National Instruments) (Fig 2B, bottom panel).
186　For length measurements, we used a Sony alpha 7s camera with an FE 2.8/90 Macro G
187　OSS lens. For the whisker diameter, we used the images taken from the
188　holotomography reconstructions. Whisker diameter was measured in a transverse
189　section close to the ring sinus, once the thickness of the initial segment of the whisker
190　reach a relatively constant thickness.
191
192　*Biomechanics*
193　Two whiskers per whisker type from three rats (P19—P25; male=2, female=1) were
194　plucked for the *ex vivo* assay (right side of the face). Whiskers were inserted by their
195　base on clay in a linear array facing the same direction. Wind came mostly from the
196　opposite direction of the resting curvature of the whiskers (see video 2). This was done
197　to maximize whisker bending and to facilitate measurements, given that we observed
198　the highest bending in this condition rather than when blowing wind in the same or
199　perpendicular directions. To prevent wind from blowing directly towards the whiskers,
200　we placed a plastic tube facing the whiskers 30 cm away from them with a fan placed
201　on the distal end of the tube, away from the whiskers (the length of the tube was ~70
202　cm) and a loose paper towel on the proximal end of the tube, near the whiskers to
203　attenuate wind intensity. The tube and the fan were approximately the same diameter
204　(15 cm). Bending angle was reconstructed by superimposing two frames of a video
205　where minimal and maximal deflection of the whisker was achieved. We used 75% of
206　the total whisker length to trace a radius centered at the base of the whisker to calculate
207　the bending angle. This procedure was repeated six times, once per whisker type. With
208　this, we obtained twelve data points per whisker type. Images were acquired using a
209　Logitech BRIO, ultra HD webcam (90 fps, Logitech).
210
211　*Cortical localization of supraorbital whisker barrels*
212　Long Evans rats (P19—P25, n=4) were anesthetized using urethane (1.4 g/kg i.p.).
213　Incised tissue was locally anesthetized with lidocaine. A rectal probe monitored body
214　temperature, and a homeothermic blanket (FHC, Bowdoinham, ME, USA) maintained
215　it at $37 \pm 0.5°C$. For facial whisker barrel experiments, a craniotomy was made above
216　the somatosensory cortex (3.5 mm posterior to Bregma; 6.5 mm lateral to Bregma).
217　Broken glass electrodes filled with Ringer solution (NaCl 135, KCl 5.4, $MgCl_2$ 1,
218　$CaCl_2$ 1.8, HEPES 5, in mM) were arranged to enter perpendicular to the cortex. Multi-
219　unit activity was amplified using an Axoclamp 2B amplifier (Axon Instruments) and
220　monitored (AM10 Grass Instruments) while moving in step coordinates centered
221　around 6.3 mm posterior and 3.8 mm lateral to Bregma, and lightly moving the
222　supraorbital whiskers.
223
224　*Neuropixel recordings and wind stimulation*
225　Male Long-Evans rats (n=3) were kept in a temperature and humidity-controlled room
226　with a 12 hr:12 hr light/dark cycle. Animals were allowed to have free access to clean
227　food and water in standard rat cages. For surgery, animals were deeply anesthetized by

228 applying intraperitoneal (ip) injections of urethane (1.5g/kg body weight (BW)). The
229 fur overlying the dorsal aspect of the animal skulls was shaved. Then the rat was placed
230 in a standard stereotaxic surgical apparatus (Narishige, Japan). The animal's body
231 temperature was measured with a rectal probe and kept at 36°C ± 0.5°C by a
232 homeothermic blanket (FHC, Bowdoinham, Me., USA). Before the surgical incision,
233 the scalp of the animal was locally anesthetized by injecting 2% lidocaine solution. To
234 access the barrel cortex, the skin was cut antero- posteriorly along the midline, and the
235 remaining connective tissue on the skull was removed. The anchoring screws were
236 inserted to the skull bone and a head-fixation post was then secured to these screws
237 using UV-curable adhesive glue (Optibond; Altschul Dental, Mainz, Germany) and
238 dental cement (Heraeus Kulzer, Hanau, Germany). Two Neuropixels probes were glued
239 together (distance between the probes 2.0 - 2.2 mm), coated with lipophilic
240 carbocyanine fluorescent dyes DiO or DiI, and lowered slowly into the barrel cortex.
241 One of the probes targeted the supraorbital whisker area at coordinates 3.8 mm posterior
242 and 6.3 mm lateral, in a way that the second probe targeted the central whisker pad.
243 Once the recording was stable, the supraorbital and wind-insensitive whiskers were
244 stimulated though mechanical and air puff means to confirm the position of both probes.
245 If no clear response was observed, that is, if no supraorbital and lower whisker pad
246 response were observed on each of the Neuropixels, the probes were then moved until
247 the expected supraorbital/whisker pad response was found. Through this procedure, one
248 of the probes showed responses exclusively during supraorbital stimulation, while the
249 second probe showed response exclusively for the wind-insensitive whiskers. Finally,
250 a vent (AITRIP, ECDG054) was positioned in front of the animal at a distance of 12.5
251 cm and low (0.5 m/s) and high (1.5 m/s) wind stimuli was presented through a balanced
252 randomized sequence of low, high and no-wind conditions (10 s each, 12 to 30 wind
253 events per rat).

254

255 *Spike Sorting*
256 Spikes were detected from the high-pass filtered data using Kilosort 3.0 (Pachitariu et
257 al., 2016) and then the output clusters manually adjusted using the "phy" gui
258 (https://github.com/cortex-lab/phylab/phy). Clusters of neurons were assessed
259 qualitatively in terms of their autocorrelogam (little presence of short-latency ISIs),
260 spike amplitude and presence of a clear waveform modulation across channels.
261 Neighboring clusters (up to 10 channels apart) were directly compared between each
262 other in terms of cross-correlogram, waveform similarity per channel, and firing rate
263 patterns (the latter, to avoid classifying as separate unit clusters that do not overlap in
264 time). Clusters with high similarity index were also compared in the same manner. Only
265 clusters satisfying all these criteria were considered in further analysis.

266

267 *Histochemical visualization of barrel patterns*
268 The animals used for whisker mapping and Neuropixels recordings were deeply
269 anesthetized and perfused transcardially with Ringer solution, followed by 4%
270 paraformaldehyde (PFA). Brains were removed, hemispheres were separated and

271 cortices were flattened between two glass slides separated by clay spacers. Glass slides
272 were weighed down with small ceramic weights for about three hours. Afterwards,
273 flattened cortices were stored overnight in 2% PFA and 80 µm sections were cut on a
274 vibratome. Sections were stained for cytochrome-oxidase activity using the protocol of
275 Wong-Riley (1979). Subsequently, barrel shapes were drawn with Neurolucida
276 software (Microbrightfield, Colchester, VT, USA) using a Zeiss Axioplan microscope
277 fitted with a 10x and 2x objective.
278
279 *Wind-sensing behavior*
280 Long Evans rats (P21—P32, male=12; female=13) were separated from littermates
281 prior to behavioral testing. Behavioral videos were recorded (Basler acA1920, 100 fps)
282 in a darkened room with the inner chamber covered with blackout curtains. The
283 behavior box was illuminated with an infrared LED lamp. Two experimenters were
284 positioned on opposing ends of the testing box and prepared for tests with hands or
285 flaps in position. Air flow measurements of hand and flap stimuli were on average ≤ 3
286 m/s and 5 m/s respectively. The testing animal was then placed in the center of the
287 chamber, and a third experimenter cued the experimental flapper by name in a random
288 sequence every 10 seconds, with a total of 20 trials per session.
289 Whisker trimming or lidocaine/Ringer injections were performed bilaterally in gently
290 restrained animals under stereoscopic magnification and illumination within 10 minutes
291 of behavior assessment. Injections were performed subcutaneously and directed to the
292 area of origin for the supra-orbital whiskers. Wind-sensitive whiskers (2 supraorbital,
293 the ear, A1, α, β and γ whiskers) or wind-insensitive whiskers (C2, C3, D2, D3, D4, E2
294 and E3) were trimmed with sharp scissors at the base of the skin without disturbing
295 other whiskers. A day prior to the actual whisker trimming/lidocaine injections, the
296 animals were habituated to the trimming/injection procedures in sham
297 trimming/injection procedures in order to minimize stress on the day of the actual
298 experiment. In such sham procedures, animals were gently restrained, positioned under
299 the microscope and a pair of scissors was brought close to the animal's face.
300
301 *Statistics*
302 Most of our dataset did not satisfy normality criteria, so we applied non-parametric
303 statistics. We analyzed data from binomial distributions with χ^2 and Fisher's exact test.
304 Mann-Whitney, Wilcoxon or Kruskal-Wallis test were employed to analyze two
305 unpaired groups, two paired groups or more than two unpaired groups, respectively.
306 Post hoc analysis was carried out using Tukey (Figure S1 and S2) or Dunn's test (Figure
307 2F). Data was expressed as the root mean square (RMS, Figure 1) or the mean ± the
308 standard error of the mean (SEM), unless indicated. We only report differences which
309 were significant and relevant to the experiment. In all cases $p < 0.05$ was the statistical
310 threshold. The analyses were done using Python 3.7 or MATLAB (MathWorks, Natick,
311 MA).
312
313 *Shuffling statistics of whisker parameters*

314 Chance-level statistics was constructed to determine an optimal arrangement for the
315 whiskers length-diameter ratio and ring-wulst aperture along the whole supraorbital-
316 whisker pad region (Figs 2D and 3F, respectively). The arrangement with the least
317 mean variance, was considered as the optimal and employed as grouping criteria for
318 further analysis.
319 Six possible arrangements were considered: arcs, rows, semicircles (from A1), oblique
320 45° (from A1), oblique 135° (from A4) and opposite semicircle (from E4). We first
321 calculated the variance inside each arrangement group (e.g., inside each semicircle) and
322 took the mean across them as an estimate of the variance of the whole arrangement. A
323 p-value for that estimation was then calculated by constructing a shuffle distribution of
324 the mean variance for that arrangement. To this aim, data points position on the pad
325 was randomized and the mean variance calculated for that arrangement. This procedure
326 was repeated 10000 times to create the shuffle distribution. Note that for both variables,
327 the semicircular arrangement exhibited the least mean variance when comparing the
328 observed value against the shuffle distribution for that arrangement.
329
330

331 **Results**

332

333 **Differential whisker displacement by airflow**

334 As a first step of our analysis, we assessed the passive displacement of whiskers by
335 wind stimuli. To this end, we filmed five heads of either deeply urethane-anesthetized
336 (n = 3) or cadaver (n = 2) rats under a variety of wind conditions. In four of the heads,
337 whisker tips with annotated whisker identity were tracked using DeepLabCut (Nath et
338 al, 2019, see also Movie 1). We identified and tracked (> 10) whiskers in all animals.
339 Accordingly, we labeled several easily identifiable whiskers, such as the long
340 supraorbitals (lSO), short supraorbitals (sSO), A-row whiskers, alpha, beta, gamma,
341 and caudal whiskers of the B and C rows (Figure 1A). We recorded videos of rats while
342 under no wind, ambient (low wind) and fan-blowing (high wind) conditions, and
343 examined the X- and Y- displacements of each whisker during the three conditions.
344 Whisker movement was minimal in the no wind condition (Figure 1B), while most
345 whiskers moved in the high wind condition (Figure 1D). Interestingly, we found that
346 during the low wind condition, only specific whiskers showed marked displacement
347 compared to the others; these were the long whiskers, predominantly the lSO, A1 and
348 α whiskers (Figure 1C, arrows). We further computed the velocity of the whisker
349 displacement (Figure 1E, F), and found maximal deflections of the long whiskers (lSO,
350 A1, α). We computed the root mean square (RMS) velocity for low wind condition
351 recordings made from 4 animals and found a consistent trend of highest RMS velocity
352 deflection for the long whiskers (Figure 1G). In all four video sequences that we
353 analyzed quantitatively we observed highly significant differences in the amount of
354 whisker displacement (measured by RMS of velocity) across whiskers (see Figure 1F).
355 While the details of whisker displacements differed across video sequences, the two
356 aspects were the same: (i) lSO, A1, α whiskers as well as closely neughboring whiskers
357 always showed big displacements; (ii) anterior and middle whiskers of the C and, D
358 rows and always showed little airflow induced displacements. These aspects are also
359 captured in our across movies analysis (Figure 1G). In addition to the quantitatively
360 analyzed movies shown in Figure 1, we also inspected a variety of additional rat head
361 movies qualitatively. These movies included videos of head side views and movies of
362 upside-down heads. All of these recordings led to similar qualitative conclusions.
363 Notably, in all of our experiments, the lSO showed very strong and usually the maximal
364 deflection, prompting us to further examine the function of the lSO in detail with
365 regards to anemotaxis in rats.

366

367 **Differential whisker biomechanics determine airflow responses**

368 We wondered how the differential responses of whiskers to airflow arise. To address
369 this question, we first visually inspected whiskers with differing airflow responses.
370 Differential characteristics were readily visible and immediately noted that the lSO
371 whisker was unusually thin for its length (Figure 2A). Such differences were confirmed
372 when we acquired micrographs of full whiskers (Figure 2B bottom) and their shafts
373 (Figure 2B top). We further characterized the detailed characteristics by plucking some

374 wind-responsive and non-wind-responsive whiskers. Total whisker length and diameter
375 were measured in wind and non-wind-engaged whiskers (Figure 2C). We computed the
376 Spearman's rank correlation coefficient to examine the relationship between whisker
377 length and base diameter, and found a positive correlation between the two variables [r
378 (26) = 0.8, p < 0.001] (Figure 2C). lSO whiskers were relatively thin and short amongst
379 the long whiskers (Arc 1, 2 and the straddlers) and display a clear difference with
380 respect to the small supraorbital and the shorter whiskers (Arc 3 and 4). We computed
381 a heatmap of the ratio between whisker length and base diameter and found that lSO
382 has the highest ratio (Figure 2D). We grouped the different whisker types according to
383 a semicircular arrangement and compared their fold change for that ratio with respect
384 to the lSO whisker. Semicircles were found to minimized the mean variance of the ratio
385 along the whisker pad when compared to other possible arrangements using shuffling
386 statistics. Further statistical analysis confirmed that lSO exhibits the highest ratio (Fig.
387 S1). This result suggests that optimal wind-engaging occurs within a length-base
388 diameter range that includes supraorbital and top semicircle whiskers. To test if whisker
389 biomechanics are indeed sufficient to determine differential airflow responses, we
390 performed *ex vivo* experiments on extracted whiskers (Figure 2E). To this end, we
391 inserted the base of a similar sample of wind and non-wind-engaged whiskers in clay
392 on a linear array with similar orientation. We calculated the maximal bending of the
393 whiskers during low wind flow with respect to the curvature at rest and took the bending
394 angle (Figure 2E–F; see methods). A Kruskal-Wallis test on whisker type showed a
395 significant effect [H (5, 42) = 36.45, p < 0.0001]. Dunn's post-hoc test indicated that
396 only comparisons involving lSO and A1 whiskers yielded significant differences.
397 Particularly, bending angle of lSO significantly differs from every other whisker (all p-
398 values < 0.02) except A1, which was another wind sensitive whisker found in our
399 previous *in vivo* assay. A1 differed from C3 and E1 (p values < 0.01). Taken together,
400 our results identify whisker biomechanics as crucial determinants of airflow responses.
401

The follicles of wind-sensitive whiskers have an unusually closed ring-wulst

403 We next compared the follicle structure of wind-sensitive and non-wind-sensitive
404 whiskers. To this end, we obtained high-resolution microCT scans of whisker follicles
405 either in situ in entire iodine-stained whisker pads or in extracted single iodine-stained
406 follicles. Our analysis was informed by the seminal work of Tonomura et al. 2015.
407 These authors identified structure-function relationships in vibrissa follicle and showed
408 that afferents with club-like endings, which are exclusively found adjacent to the ring-
409 wulst, are the most sensitive follicle afferents with the highest discharge rates. We
410 reckon that such ring-wulst afferents are most likely to respond to wind stimuli, which
411 do not even evoke a visible deflection in many whiskers. We show a volume rendering
412 of the follicle of the long supra-orbital whisker follicle, a highly wind-sensitive whisker
413 in Figure 3A and of the E1 whisker follicle, a non-wind-sensitive whisker in Figure 3B.
414 The two whiskers differ in their ring-wulst, which we reconstructed via manual
415 segmentation, high-lighted by color in the volume image and which we show in
416 isolation in Figure 3C. Wind-sensitive whiskers have relatively closed ring-wulst
417 (Figure 3C), whereas non-wind-sensitive whiskers tend to have an open ring-wulst

418   (Figure 3D). Population data on ring-wulst opening are plotted in Figure 3E—F. Note
419   the similarity of 'ring-wulst-closedness' (Figure 3E) and wind-induced deflection as
420   shown in Figure 1. A heat map of ring wulst aperture angles indicate the most closed
421   aperture in lSO and sSO follicles, while the most open aperture conformations are found
422   in E-row and arch-4 follicles (Figure 3F). We grouped the different whisker types
423   according to a semicircular arrangement and compared their fold change for the ring-
424   wulst aperture with respect to the lSO whisker. Semicircles were found again to
425   minimized the mean variance when compared to other possible arrangements using
426   shuffling statistics, but this time for the ring-wulst aperture. Further statistical analysis
427   confirmed that lSO exhibits the closest ring-wulst (Fig. S2A). Interestingly, we found
428   that the ratio between whisker length and diameter (but not if taken separately) was
429   inversely correlated with the ring-wulst aperture, this is: the closest the ring-wulst, the
430   highest the ratio (Fig. S2B). We conclude that the follicles of wind-sensitive whiskers
431   differ by an unusually closed ring-wulst from non-wind-sensitive whiskers.
432
433   **Mapping of supra-orbital whisker barrels and relation of whisker airflow**
434   **displacement to the cortical barrel map**
435   The differential mechanical airflow responses of whiskers point towards a role of the
436   supraorbital whiskers in airflow sensing. We therefore mapped the location of cortical
437   barrels representing the supraorbital whiskers in extracellular receptive field mapping
438   experiments and prepared cytochrome oxidase sections of layer 4 of the barrel cortex
439   (Figure 4A). We consistently (in four out of four mapping experiments) observed
440   supraorbital whisker responses in brain regions posterior to the A1 and α whisker
441   response areas. Also, the stereotaxic coordinates of supraorbital whiskers were highly
442   consistent (6.26 ± 0.01 mm lateral and 3.75 ± 0.20 mm posterior to bregma, mean $\pm$
443   standard error of the mean). These observations led us to a suggestion for the location
444   of the supraorbital whisker barrels in relation to the rest of the barrel field (Figure 4B).
445   Next, we wondered how mechanical airflow responsivenss relates to the cortical barrel
446   field and we color coded it and superimposed to the barrel map (Figure 4C).
447   Quantitative tracking data for whisker displacement was not available for all whiskers
448   (hence the empty barrels), but it was nonetheless clear that wind-responsive whiskers
449   (with large air flow displacements) cluster in the posterolateral barrel map.
450   We also inspected the putative supraorbital whisker barrels in many (n = 10) additional
451   barrel maps that we derived for other purposes in previous studies (Lenschow et al
452   2016; Lenschow, Sigl-Glöckner, & Brecht 2017). We made the following observations:
453   (i) the exact position and orientation of putative supraorbital whisker barrels relative to
454   the posteromedial-barrel-subfield is somewhat variable and more variable relative to
455   the position and orientation of the mystacial barrels to each other. (ii) Putative
456   supraorbital whisker barrels are elongated. (iii) Putative supraorbital whisker barrels
457   are always close (see also Figure 4A–B). (iv) The septum separating putative
458   supraorbital whisker barrels is weaker than the septum separating mystacial barrels (see
459   also Figure 4A–B). The latter two observations support the idea that the short and long
460   supraorbital whiskers are functionally related.
461

462 **Neurons in the supra-orbital whisker representation responds more strongly to**
463 **wind stimuli than E/D-row barrel cortex neurons**
464 Next, we wondered if the cortical supra-orbital whisker representation differed from
465 barrel cortex neurons in their responses to wind stimuli. To this end, we applied wind
466 stimuli to urethane-anesthetized rats, while recording simultaneously with Neuropixel
467 probes from the supra-orbital whisker region at the coordinates identified in our
468 mapping experiments and from the whisker pad region aiming towards E/D-row barrel
469 cortex (Figure 5A). We histologically confirmed recording locations to the supraorbital
470 cortical region and the whisker pad barrel cortex near E/D-row (Figure 5B). Judging by
471 the population peri-stimulus time histogram (PSTH), there was not much of a wind-
472 evoked response in recordings from E/D-row barrel cortex. In contrast, there was a clear
473 excitatory response in the supra-orbital whisker region (Figure 5C). Plots of the z-
474 scored responses of individual neurons revealed either no, weak, or inhibitory responses
475 to wind-stimuli in E/D-row barrel cortex. In the supra-orbital whisker region, we
476 observed strong excitatory responses in single cells (Figure 5D). The differences in
477 wind responses between the supra-orbital region and the whisker pad region were
478 highly significant (Figure 5E) and distributed differently across response categories
479 (Figure 5F). We conclude that wind responses map to the supra-orbital whisker
480 representation.
481
482 **Anemotaxic turning in rats**
483 To assess the behavioral capacities for wind-sensing in rats, we developed an airflow
484 sensing paradigm. To this end, we placed a rat in a box with three compartments
485 separated by wire-mesh in total darkness, i.e., the box was shielded in a rack with dark
486 curtains and additionally experiments were conducted in a darkened room. Videos were
487 acquired using an infrared (IR) light and an IR camera, both positioned above the
488 experimental box. The rats were placed in the middle compartment and two
489 experimenters performed repetitive hand-flaps or card-flaps, in either one of the two
490 lateral compartments (Figure 6A, C). Air flow measurements of hand and flap stimuli
491 were on average ≤ 3 m/s and 5 m/s respectively, measured with an anemometer. The
492 reactions of rats to hand-flap stimuli (presented randomly every 10 seconds on either
493 side of the box) were assigned by forced choice to one of three categories: either no
494 reaction or turning towards the stimulus or turning away from the stimulus. (Figure
495 6B). Even though rats often showed no reaction, when they did, the animals appeared
496 to be able to distinguish the side where the hand-flap was delivered. Accordingly, rats
497 turn significantly more often towards hand-flaps than away from them (Fig. 6B;
498 $p<0.001$, χ^2 Test; 'Turn to' (31 trials) vs 'Turn away' (7 trials)). Next, we wanted to
499 compare the rats' reactions to different wind stimuli. Using the same behavioral
500 paradigm, we changed the wind delivering method by flapping a cardboard piece,
501 which evokes a more powerful airflow than the hand-flap (Fig. 6C). Again, the animals
502 consistently showed a higher percentage of responses towards the stimuli side when
503 compared to turning away responses (Fig. 6D; $p<0.001$, χ^2 Test). Strikingly, when
504 comparing the 'Turn to' responses in the two wind delivery methods, we observed a
505 stronger reactivity of the animals to cardboard-flap than to hand-flap stimuli (Fig. 6C,

506   D; p=0.0036, Fisher's Exact Test). Our results show that rats can not only sense, but
507   also turn to airflow stimuli. The strength of the reactions differed between weak (hand-
508   flap) and strong (cardboard-flap) stimuli. Since we carefully avoided noises associated
509   to hand-flap or cardboard-flap stimuli and conducted experiments in total darkness, it
510   is likely that animals indeed sensed airflow. The whisker trimming and lidocaine
511   injection effects described below show the turning responses observed were indeed at
512   least partially if not entirely tactile reactions.
513

Wind-whisker trimming and supraorbital whisker blockade interfere with airflow
514
turning responses
515
516   Wind-responsive whiskers (2 supraorbitals, ear, A1, α, β and γ whiskers), as identified
517   in our whisker tracking experiments, were trimmed in 7 rats (Figure 7A). A subset of
518   wind-insensitive whiskers (C2, C3, D2, D3, D4, E2 and E3) were trimmed in 7 different
519   rats, which had their wind-responsive whiskers intact (Figure 7B). Both sets of
520   individuals were then submitted to cardboard-flap stimuli in complete darkness and
521   were filmed (Figure 7C), as described in the previous section. Out of 20 trials, we
522   counted each individual's number of turns towards the stimulus. We found that on
523   average, wind-whisker-trimmed individuals turned towards the stimulus 20% of the
524   time, while non-wind-whisker-trimmed individuals turned towards the stimulus 29%
525   of the time (p=0.02, Figure 7D). Thus, removal of wind-responsive whiskers resulted
526   in a stronger decrease in turning behavior than the removal of wind-insensitive
527   whiskers.
528   We next asked if supraorbital whiskers alone play a role in wind-induced turning. To
529   investigate this, we injected 8 individuals with either lidocaine or Ringer solution (as a
530   negative control) locally at their supraorbital whisker follicles and followed this with
531   an injection of the respective other solution 24 hours later (Figure 7E). After each
532   injection, we subjected the animals to the cardboard-flap tests, as illustrated in Figure
533   5C. Therefore, we have 8 paired trials for each condition. Seven out of eight individuals
534   showed a decrease in turning behavior for lidocaine when compared with Ringer
535   solution (Figure 7F). The average turns towards the cardboard-flap stimulus were less
536   frequent (18%) for lidocaine treatment than for Ringer treatment (23%, p=0.039). We
537   conclude that supraorbital whiskers alone contribute significantly to airflow turning
538   responses.
539

540   **Discussion**

541

542   **Summary**

543   We studied rat anemotaxis by combining whisker tracking, biomechanical analysis of
544   whisker airflow responses, follicle analysis, somatosensory cortex recordings,
545   behavioral analysis of airflow turning and whisker interference by trimming and
546   lidocaine injections. This diversity of methods led to a coherent pattern of results.
547   Whiskers greatly differ in their airflow sensitivity and strongly wind-responsive
548   whiskers – in particular the long supraorbital whiskers – determine behavioral
549   responses to airflow stimuli in rats.

550

551   **Differential sensitivity of rat whiskers and downstream cortices to airflow**
552   Whisker tracking of large numbers of whiskers (>10) under a variety of airflow
553   conditions suggested differential sensitivity of rat whiskers to airflow. The sheer
554   amount of data acquired here reflects the power of tracking software such as
555   DeepLabCut (Mathis et al. 2018; Mathis & Mathis 2020) without which our analysis
556   would not have been possible. The patterns of whisker airflow displacement were
557   remarkably consistent across experiments. First, no airflow (shielded) conditions
558   largely abolished whisker displacement in anesthetized and cadaver animals, showing
559   that it is indeed airflow that leads to whisker tip displacement. Second, we found that
560   strong airflow displaces all whiskers. Third, low airflow conditions lead to a differential
561   engagement of whisker tips, with some whiskers (in particular the supraorbitals)
562   showing strong movements. The 'low' airflow conditions studied here included simply
563   ambient airflow in a room with air conditioning or – in a closet – the turning on of a
564   fan that was not directly aimed towards the whiskers. We realize that such airflow
565   conditions are not strictly controlled, but they provided nonetheless the most interesting
566   results, namely very strong whisker displacements in some whiskers (but not others),
567   when one 'feels' barely any or no wind. Data on more controlled airflow whisker
568   displacements were gathered by Yu, Graff & Hartmann (2016). We think both
569   controlled airflow whisker displacements as pioneered by Yu, Graff & Hartmann
570   (2016) and the study of ambient naturalistic airflow as done here provide information
571   about whisker airflow responses.
572   Our biomechanical analysis enforced the idea of a differential whisker sensitivity to
573   airflow. First, we found that strongly airflow responsive whiskers such as the
574   supraorbital and the A1 whiskers are very thin. Second and more interestingly, even the
575   extracted long supraorbital whisker shows exceptionally strong airflow responses,
576   partially due to a high whisker length-diameter ratio. The follicles of wind-sensitive
577   whiskers differ from non-wind-sensitive whiskers by a more closed ring-wulst. Such
578   ring-wulst differences are of great functional interest, because club-like endings on the
579   ring-wulst are thought to form the most sensitive whisker afferents (Tonomura et al.
580   2015). A synopsis of our observations points towards biomechanical specializations
581   that endow the supraorbital whiskers with strong airflow omni-directional sensing.
582   Cortical recordings confirmed – in direct comparison with whisker pad region – that
583   the supraorbital region is particularly wind-sensitive.

584

Rat anemotaxis

586 Previous work by Yu et al. (2016) established the ability of rats to sense windblown
587 through tunnels. These abilities were diminished by trimming all facial whiskers (Yu
588 et al. 2016). Our current work extends our knowledge of rat anemotaxic abilities. We
589 demonstrate that rats show robust turning responses to both weak (hand-flaps) and
590 strong (cardboard-flaps) airflow stimuli. Such turning responses confirm that rats can
591 not only detect but also localize airflow stimuli. The task conditions (total darkness, no
592 contact/little or no audible sounds) and the diminished airflow responsiveness after
593 whisker trimming or blockade clearly indicate that tactile stimuli induce anemotaxic
594 turning. At least for the hand-flap, the evoked airflow currents – which the animals
595 detect in distances of 10cm or more – is small (measured airflow ≤ 3 m/s). Since a hand-
596 flap is not categorically different from airflows induced by biologically relevant stimuli
597 (such as a predator), we think such anemotaxic sensing might offer real-world
598 advantages to nocturnal animals like rats. With the exception of the fact that rats turn
599 towards rather than away from hand-flap stimuli, our observations remind us of
600 anemotaxic escape behaviors as they have been described in insects. Indeed, we wonder
601 if the rat's anemotaxic turning observed by us is also a defensive behavior that guards
602 the animal against surprise attacks from the side or behind. The idea that supraorbital,
603 A1 and α whiskers mediate defensive behaviors matches with their representation in
604 the medial superior colliculus (Dräger & Hubel 1975), where both visual (Yilmaz &
605 Meister 2013) and electric stimulation (Dean, Redgrave & Westby 1991) evoke
606 defensive behaviors such as escape and freezing.

607 Independent of exact purpose and the underlying neural circuits, we find that
608 anemotaxic turning is an extremely valuable behavioral assay for wind-sensing in rats.
609 As it requires no prior conditioning, the robustness of the behavior allowed us to screen
610 wind-sensing abilities in large numbers (> 20) of rats.

611

The supraorbital whiskers as wind antennae

613 The central conclusion from our work is that whiskers differ in their sensitivity to
614 airflow stimuli. Specifically, the supraorbital whiskers emerged as key sensors for wind
615 stimuli from our analysis. These whiskers show maximal displacement to weak airflow
616 stimuli, a response property that – according to *ex vivo* experiments – reflects the unique
617 biomechanical properties of these whiskers. The very dorsal position, and the upward
618 bending very likely further enhances airflow sensitivity. At least in mice, supraorbital
619 whiskers appear to be actively whisked together with the mystacial whiskers (Severson
620 et al. 2019). The two supraorbital whiskers are represented in two closely adjacent
621 cortical barrels. Both whisker trimming and most of all the effects of lidocaine
622 injections document the functional significance of supraorbital whiskers for airflow
623 sensing. The reduction of anemotaxic turning after supraorbital lidocaine injections is
624 a remarkable result, given that these bilateral injections targeted only 4 out of the
625 roughly 300 rat whiskers.

626

627

Conclusion

628

629 Our data adds to the growing evidence that the functional diversity of whiskers enriches

630 the rat's sensory world (Diamond et al. 2008, Szwed et al 2003). The much-studied

631 mystiacial macrovibrissae seem to serve many functions, the microvibrissae mediate

632 object contacts, trident whiskers engage in ground sensing and supraorbital whiskers –

633 according to several lines of evidence provided here – act as wind whiskers.

634

635   **References**

636

637   Anjum F, Turni H, Mulder PG, van der Burg J, Brecht M (2006) Tactile guidance of
638   prey capture in Etruscan shrews. Proc Natl Acad Sci U S A 103: 16544-16549.

639

640   Brecht M, Preilowski B, Merzenich MM (1997) Functional architecture of the
641   mystacial vibrissae. Behavioural Brain Research 84: 81-97.

642

643   Brecht M (2007) Barrel cortex and whisker-mediated behaviors. Current Opinion
644   Neurobiology 17: 408-16.

645

646   Chapin JK, Lin CS (1984) Mapping the body representation in the SI cortex of
647   anesthetized and awake rats. J Comp Neurol 229:199-213.

648

649   Chorev, E., Preston-Ferrer, P., & Brecht, M. (2016). Representation of egomotion in
650   rat's trident and E-row whisker cortices. *Nature neuroscience*, *19*(10), 1367-1373.

651

652   Dean, P., Redgrave, P., & Westby, G. M. (1989). Event or emergency? Two response
653   systems in the mammalian superior colliculus. *Trends in neurosciences*, *12*(4), 137-
654   147.

655

656   Diamond, Mathew E., et al. "'Where'and'what'in the whisker sensorimotor system."
657   Nature Reviews Neuroscience 9.8 (2008): 601-612.

658

659   Dräger, U. C., & Hubel, D. H. (1975). Responses to visual stimulation and
660   relationship between visual, auditory, and somatosensory inputs in mouse superior
661   colliculus. *Journal of Neurophysiology*, *38*(3), 690-713.

662

663   Elston GN, Pow DV, Calford MB (1997) Neuronal composition and morphology in
664   layer IV of two vibrissal barrel subfields of rat cortex. Cerebral Cortex 7:422–431.

665

666   Grant, R. A., Mitchinson, B., Fox, C. W., & Prescott, T. J. (2009). Active touch sensing
667   in the rat: anticipatory and regulatory control of whisker movements during surface
668   exploration. Journal of neurophysiology, 101(2), 862-874

669

670   Jadhav, Shantanu P., and Daniel E. Feldman. "Texture coding in the whisker system."
671   Current opinion in neurobiology 20.3 (2010): 313-318.

672

673   Jovanic, T., Winding, M., Cardona, A., Truman, J. W., Gershow, M., & Zlatic, M.
674   (2019). Neural substrates of Drosophila larval anemotaxis. *Current Biology*, *29*(4),
675   554-566.

676

677   Kalmus, H. (1942). Anemotaxis in Drosophila. *Nature*, *150* (3805), 405-405.

678

679 Landolfa, M. A., & Miller, J. P. (1995). Stimulus-response properties of cricket cereal
680 filiform receptors. *Journal of Comparative Physiology A*, *177*(6), 749-757.
681

682 Lenschow, C., Copley, S., Gardiner, J. M., Talbot, Z. N., Vitenzon, A., & Brecht, M.
683 (2016). Sexually monomorphic maps and dimorphic responses in rat genital
684 cortex. *Current Biology*, *26*(1), 106-113.
685

686 Lenschow, C., Sigl-Glöckner, J., & Brecht, M. (2017). Development of rat female
687 genital cortex and control of female puberty by sexual touch. *PLoS biology*, *15*(9),
688 e2001283.
689

690 Mathis, A., Mamidanna, P., Cury, K. M., Abe, T., Murthy, V. N., Mathis, M. W., &
691 Bethge, M. (2018). DeepLabCut: markerless pose estimation of user-defined body
692 parts with deep learning. *Nature neuroscience*, *21*(9), 1281-1289.
693

694 Mathis, Mackenzie Weygandt, and Alexander Mathis. "Deep learning tools for the
695 measurement of animal behavior in neuroscience." *Current opinion in*
696 *neurobiology* 60 (2020): 1-11.
697

698 Metscher, B.D., (2009). MicroCT for comparative morphology: simple staining
699 methods allow high-contrast 3D imaging of diverse non-mineralized animal tissues.
700 *BMC Physiol*. 9: p. 11.
701

702 Nath, T., Mathis, A., Chen, A. C., Patel, A., Bethge, M., & Mathis, M. W. (2019).
703 Using DeepLabCut for 3D markerless pose estimation across species and
704 behaviors. *Nature protocols*, *14*(7), 2152-2176.
705

706 Severson, K. S., Xu, D., Yang, H., & O'Connor, D. H. (2019). Coding of whisker
707 motion across the mouse face. *Elife*, *8*, e41535.
708

709 Suver, M. P., Matheson, A. M., Sarkar, S., Damiata, M., Schoppik, D., & Nagel, K. I.
710 (2019). Encoding of wind direction by central neurons in Drosophila. *Neuron*, *102*(4),
711 828-842.
712

713 Szwed M, Bagdasarian K, Ahissar E (2003) Encoding of Vibrissal Active Touch.
714 Neuron 40:621–630.
715

716 Tauber, E. R. A. N., & Camhi, J. (1995). The wind-evoked escape behavior of the
717 cricket Gryllus bimaculatus: integration of behavioral elements. *The Journal of*
718 *experimental biology*, *198*(9), 1895-1907.
719

720 Thé L, Wallace ML, Chen CH, Chorev E, Brecht M (2013) Structure, function, and
721 cortical representation of the rat submandibular whisker trident. *J*
722 *Neurosci* 33(11):4815-24.
723

724   Tonomura, S., Ebara, S., Bagdasarian, K., Daisuke, U. T. A., Ahissar, E., Inbal, M. E.
725   I. R., ... & Kumamoto, K. (2015). Structure-function correlations of rat trigeminal
726   primary neurons: Emphasis on club-like endings, a vibrissal
727   mechanoreceptor. *Proceedings of the Japan Academy, Series B*, *91*(10), 560-576.
728
729   Woolsey TA, Van Der Loos H (1970) The structural organization of layer IV in the
730   somatosensory region (SI) of mouse cerebral cortex. The description of a cortical field
731   composed of discrete cytoarchitectonic units. Brain Research 17:205–242.
732
733   Yan, S. W., Bush, N. E., & Hartmann, M. J. (2019). Whisker vibrations and the
734   activity of trigeminal primary afferents in response to airflow. *Journal of*
735   *Neuroscience*, *39*(30), 5881-5896.
736
737   Yilmaz, M., & Meister, M. (2013). Rapid innate defensive responses of mice to
738   looming visual stimuli. *Current Biology*, *23*(20), 2011-2015.
739
740   Yu, Y. S., Graff, M. M., Bresee, C. S., Man, Y. B., & Hartmann, M. J. (2016).
741   Whiskers aid anemotaxis in rats. *Science Advances*, *2*(8), e1600716.
742
743   Yu, Y. S., Graff, M. M., & Hartmann, M. J. (2016). Mechanical responses of rat
744   vibrissae to airflow. *Journal of Experimental Biology*, *219*(7), 937-948.
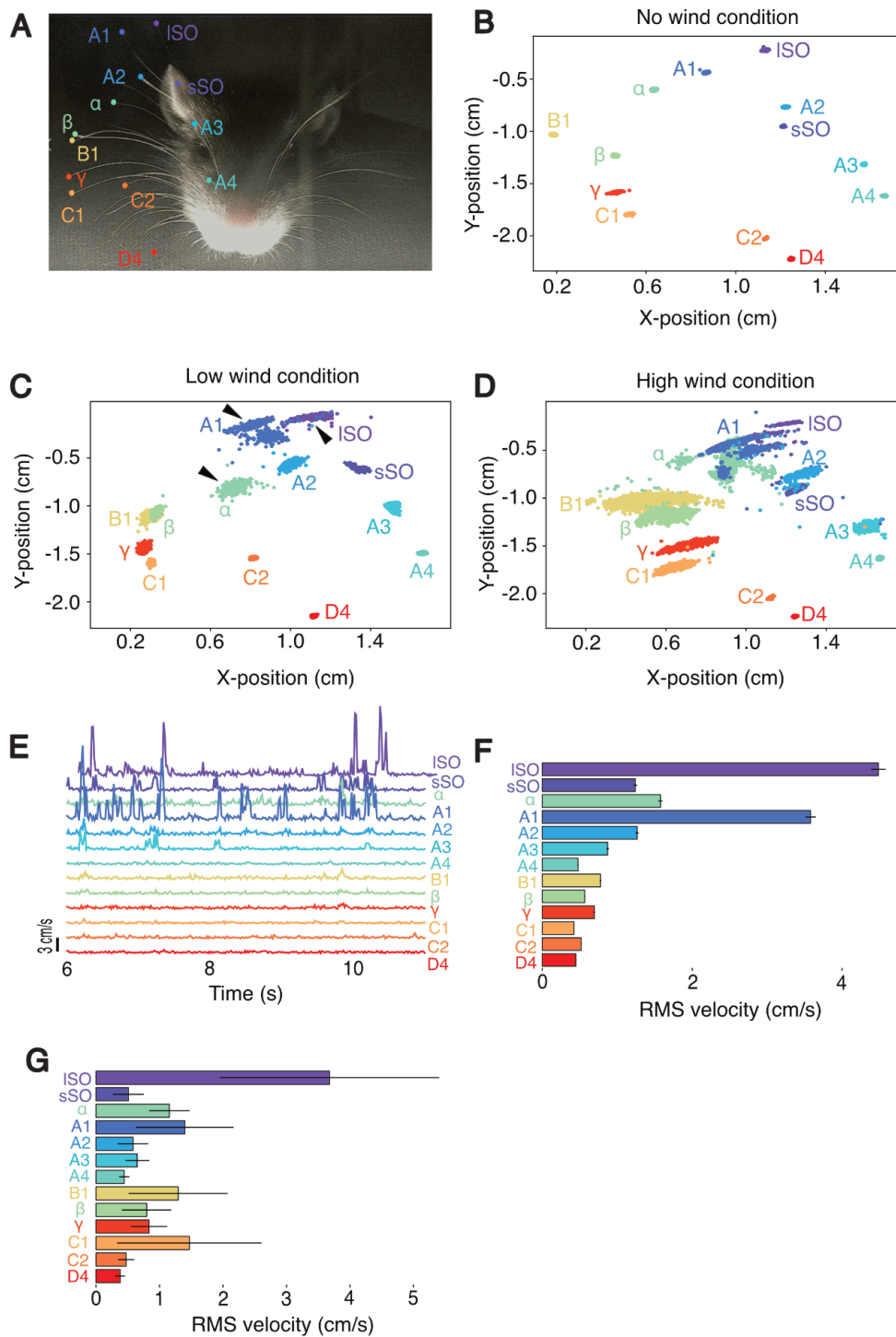745
746

764   **Figures**

765

766   **Figure 1. Differential displacement of rat whiskers responses to air flow**

767   *A,* Head of a deeply anesthetized rat with whisker tips tracked by DeepLabCut. (See

768   also Movie 1).

769   **B,** Tracked X- and Y-coordinates of whisker tips under no airflow conditions, i.e., when
770   the rat head was filmed in a small (ca. 1.5 m^2) locked closet. Whiskers are stationary
771   during the no wind condition.
772   ***C,*** Tracked X- and Y-coordinates of whisker tips under low airflow conditions, i.e.,
773   when the rat head was filmed in a small (ca. 1.5 m^2) closet with fan turned on at its
774   lowest speed, and was directed away from the head. Whiskers are stationary during the
775   no-wind condition. Note the selective deflection of long supraorbital (lSO), A1 and α
776   whiskers (black arrows) during the low wind condition.
777   ***D,*** Tracked X- and Y-coordinates of whisker tips under high airflow conditions, i.e.
778   when the rat head was filmed with the fan directed to the head.
779   **(E),** Example velocity traces for all labeled whiskers during the low wind condition
780   shown in **(C)**.
781   **(F),** Root mean square (RMS) velocity ± SEM for all tracked whiskers in the low wind
782   condition shown in **(C)**. Differences in RMS values across whiskers were statistically
783   highly significant ($p < 0.000001$; non-parametric one-way ANOVA).
784   **(G)** RMS velocity ± SEM across several animals (n = 4 animals), shows consistent
785   deflection of the lSO in low wind conditions.
786

787
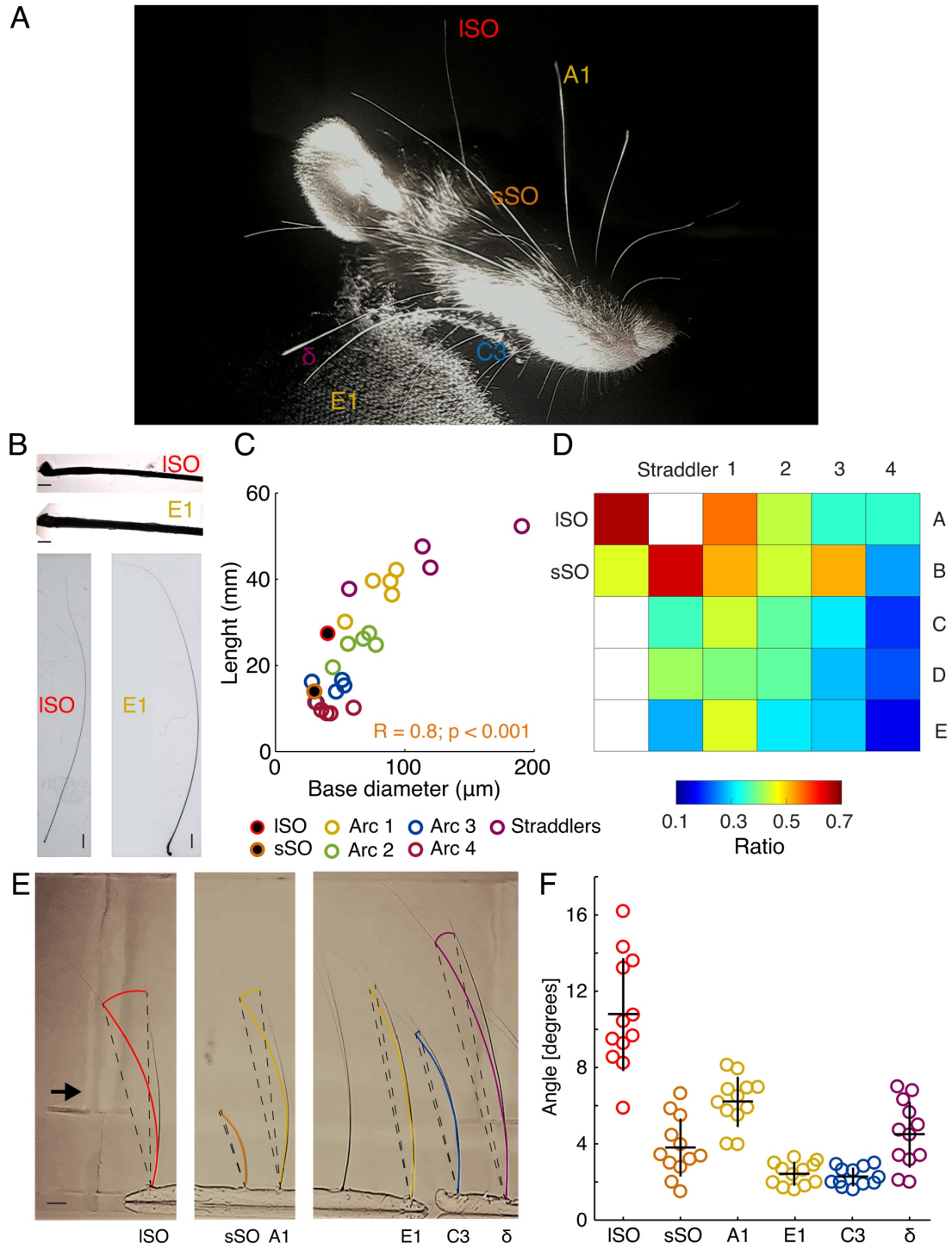
788

789   **Figure 2. Differential biomechanics determine rat whiskers air flow responses**

790   *A*, Head of a deeply anesthetized rat. Note the thin whisker diameter of the long supra-

791   orbital (lSO) whisker.

792   *B*, Micrograph of the initial segments of lSO and E1 whiskers (top). Photograph of lSO

793   and E1 whiskers (bottom). Scale 1 mm. Scale 100 μm.

794   *C*, Whisker length plotted against whisker base diameter. Color coded by arcs, inside

795   which length vary the less. Each data point represents the mean length or diameter of

796   each whisker type (n = 4). Spearman correlation indicated.

797   *D*, Heatmap of the ratio between whisker length and base diameter. Note that lSO has

798   the highest ratio (see Fig. S1).

799   *E*, Whisker bending while blowing wind onto extracted whiskers *ex vivo*. Note:

800   supraorbital whiskers and high and low length/diameter ratio whiskers where

801   subsampled from the whisker pad. Bending angle was reconstructed by superimposing

802   two frames of a video where minimal (rest, left) and maximal (full deflection, right)

803   deflection in one whisker was achieved. In this picture, maximal lSO bending is shown.

804   Color coded curves were drawn to fit 75% of the total whisker length. This partial

805   length was employed to trace a radius (dashed lines) centered at the base of the whisker

806   to calculate the bending angle. Approximate wind direction (black arrow). Scale 2 mm

807   (black line, bottom left).

808   F, Bending angle for each whisker type (color coded). Each dot represents the

809   deflection that a given whisker reached when itself or other whisker type reached its

810   maximal bending. Kruskal-Wallis test on whisker type [$H_{(5, 42)} = 36.45$, $p < 0.0001$].

811   Dunn's post-hoc test indicated that the lSO bending angle significantly differed from

812   every other whisker (All ps < 0.02) except from A1. Meanwhile, A1 differed from C3

813   and E1 (ps < 0.01). Black crosses indicate the mean and standard error.

814

815   See also Movie 2.

816

817
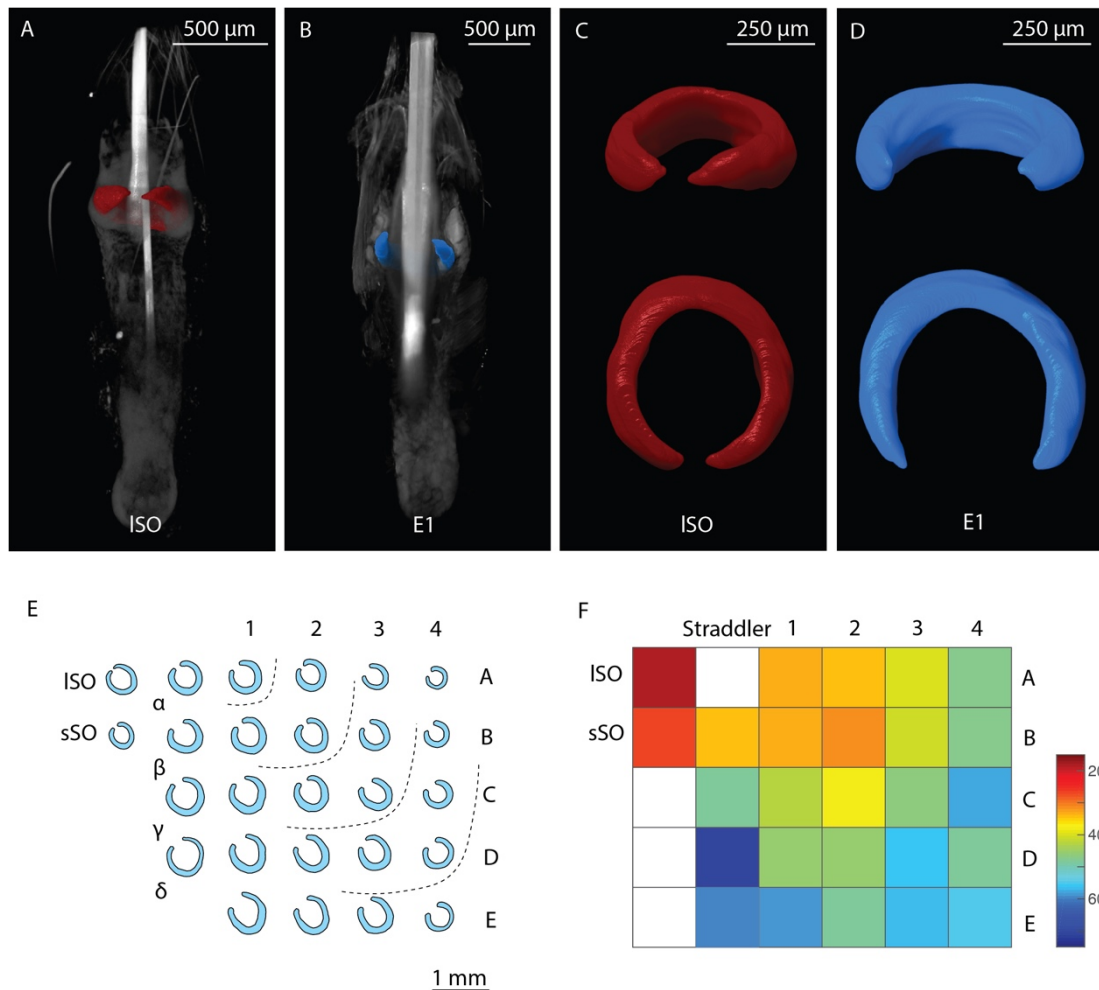
818
819 **Figure 3. Supraorbital whiskers and other wind-sensitive whisker have more**
820 **closed/ complete ring-wulst than non-wind-sensitive whiskers**
821 *A,* Micro-CT scan volume rendering of a large supra-orbital (lSO) vibrissa follicle.
822 Gross anatomy is vizualized in grey and ring-wulst reconstructions in color (red).
823 *B,* As (**A**) but for the E1 vibrissae follicle (blue ring wulst).
824 *C,* Reconstructed lSO ring-wulst from (A) in an oblique and top view.
825 *D,* Same as (C) but for the E1 follicle from (B). Note the markedly difference in the
826 ring-wulst aperture angle between the wind sensitive lSO and non-wind sensitive E1
827 vibrissa.
828 *E,* Illustration of vibrissa ring-wulst shapes drawn from micro-CT scans. Dotted lines
829 indicate a semi-circle like arrangement of vibrissae by ring-wulst aperture angles.
830 *F,* Heat map of ring-wulst aperture angles. Measurements were taken from the center
831 of the (new) hair shaft to the most distal extension of the ring-wulst in the plane of
832 maximum aperture (n = 5). Color bar indicates closed (red) to rather open (blue)
833 conformations.
834
835
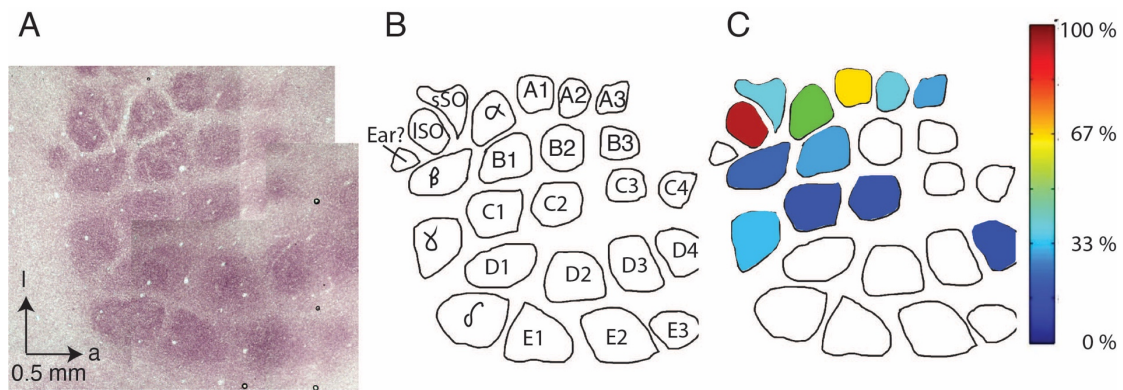
Figure 4. Localization of supraorbital whisker barrels and relation of whisker airflow displacement to the cortical barrel map

A, Cortical barrels in a tangential section through layer 4 of rat barrel cortex revealed staining for cytochrome oxidase reactivity; dark brown color indicates high reactivity. a = anterior, l = lateral.

B, Drawing of cortical barrels (from *A*) with the positions of supraorbital whisker barrels. Short (sSO) and long (lSO) supraorbital whisker barrels were identified in four receptive field mapping experiments, in all cases posterior rather than lateral to α/A1 whisker responses. Note that some anterior barrels (A4 and B4) and microvibrissae barrels are missing due to sectioning.

C, Whisker displacement under low airflow conditions was quantified, normalized to the maximal response, color coded and superimposed to the barrel map drawn in *B*. The data come from an airflow whisker displacement experiment on the head of the anesthetized animal analogous to the data shown in Figure 1F. Quantitative tracking data for whisker displacement were not available for all whiskers (hence the empty barrels). Qualitative assessment of D- and E-row whiskers suggested they show little air flow whisker displacement similar to the data of whisker D4 (also see Movie 1). Wind-responsive whiskers (with large airflow displacements) cluster in the posterolateral barrel map.
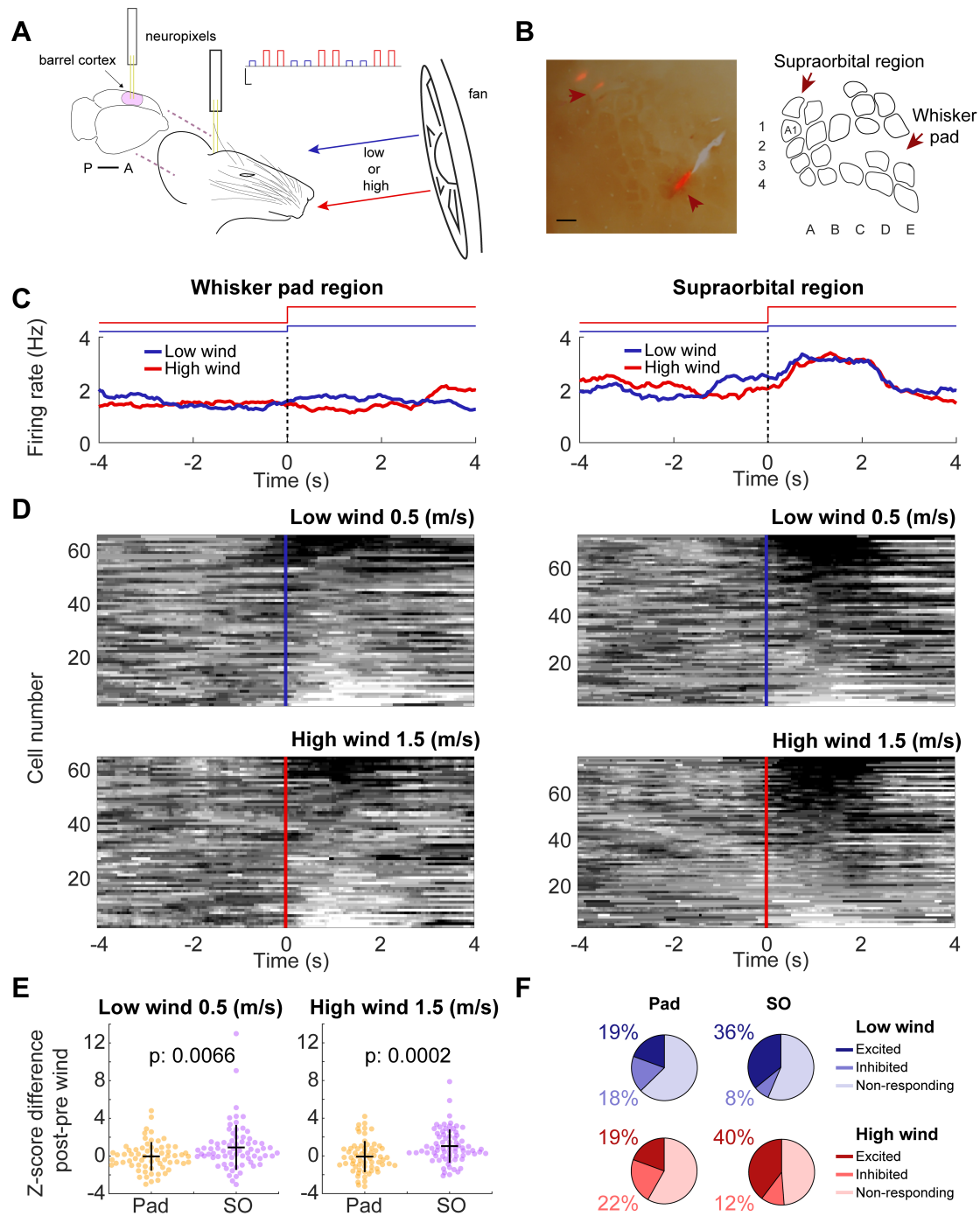
Figure 5. Supraorbital whisker cortex responds more strongly to wind stimuli than D/E-row barrel cortex

A, Schematic of the experimental setup. Posteriorly and anteriorly placed Neuropixels probes were aimed to the supraorbital and the whisker pad regions of the barrel cortex, respectively. Simultaneous, contralateral recording of single units were made while blowing wind. Low (0.5 m/s, blue) or high (1.5 m/s, red) wind epochs (10 s) were blown in alternating order from a frontal fan placed 12.5 cm apart from the rat's head. Top right: schematic of the wind epochs in time (12-30 total wind epochs per rat). Scales, x: 10 s; y: 1.5 m/s.

870   **B,** Left: representative histology showing the two recording sites on the whisker pad
871   and supraorbital regions of the barrel cortex. Scale: 500μm. Right: schematic
872   reconstruction of the barrel cortex from successive flattened brain slices.
873   **C,** Representative examples of peri-wind stimulus firing rate of two single units
874   recorded at the whisker pad (left) or supraorbital (right) regions in the low (blue) and
875   high (red) wind conditions. Black dash lines and color code step lines on top indicate
876   stimuli onset.
877   **D,** Heatmap of z-scored firing rate around wind stimuli (low wind, up; high wind,
878   bottom) of single units recorded at the whisker pad (left) or supraorbital (right) regions.
879   Positive z-scores indicate excitation (black). Negative z-scores indicate inhibition
880   (white).
881   **E,** Z-scored firing rate for the difference between post vs. pre-wind stimulation in single
882   units recorded at the whisker pad (yellow) or the supraorbital (lilac) regions for low
883   (left) and high (right) wind conditions.
884   **F,** Percentages of excited ($x > 1$ std), inhibited ($x < 1$ std) and non-responding (1 std $>$
885     $x < 1$ std) single units recorded at the whisker pad (left) or supraorbital (right) regions
886   in the low (blue) and high (red) wind conditions.
887
888
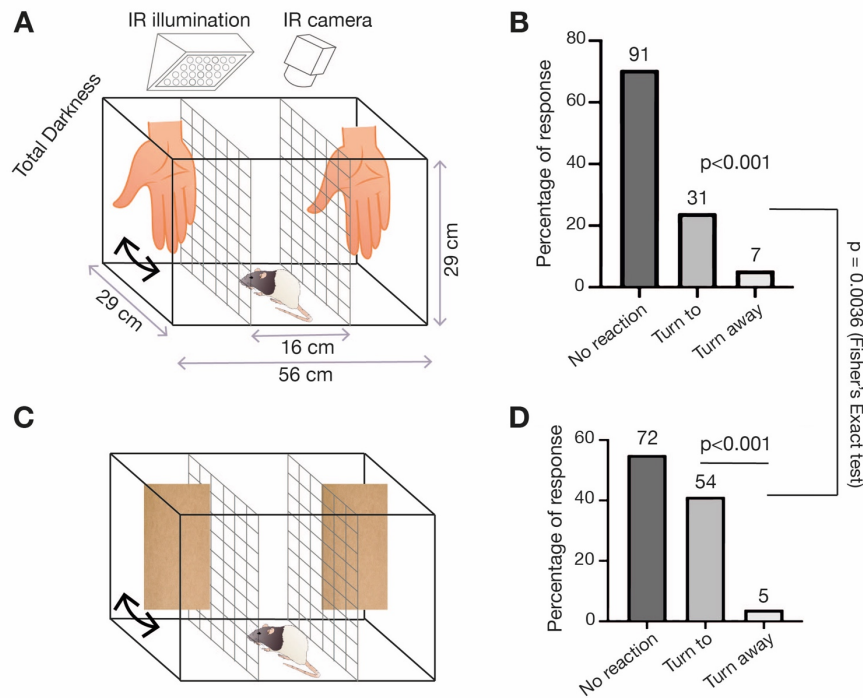
Figure 6. Anemotaxic turning in rats

A, The turning behavior arena is split into 3 sections separated by wire-mesh. The rat is placed in the middle compartment and airflow stimuli is applied by hand-flap in the left and right compartments. Left and right hand-flap stimuli were randomized and separated by 10 seconds each. The arena was illuminated with infrared light and filmed with an infrared-sensitive camera in total darkness.

B, Behavioral responses of rats (n = 7) to hand-movement stimuli (0.5 seconds post stimulus) were assigned by forced choice to one of three categories: either no reaction or turning towards the stimulus or turning away from the stimulus. Rats were strongly biased to turn towards the hand-movement stimuli (p<0.001, χ^2Test).

C, Cardboard-flaps are used to apply stronger airflow stimuli than the hand-flaps; the stimulation protocol is as in *A*.

D, Seven rats react to cardboard-flap movement stimuli from (C), scoring is done as in *B*. Rats were strongly biased to turn towards the hand-flap stimuli (p<0.001, χ^2 Test). Rats turn towards cardboard-flaps more frequently than to hand-flaps (p=0.0036, Fisher's Exact Test).
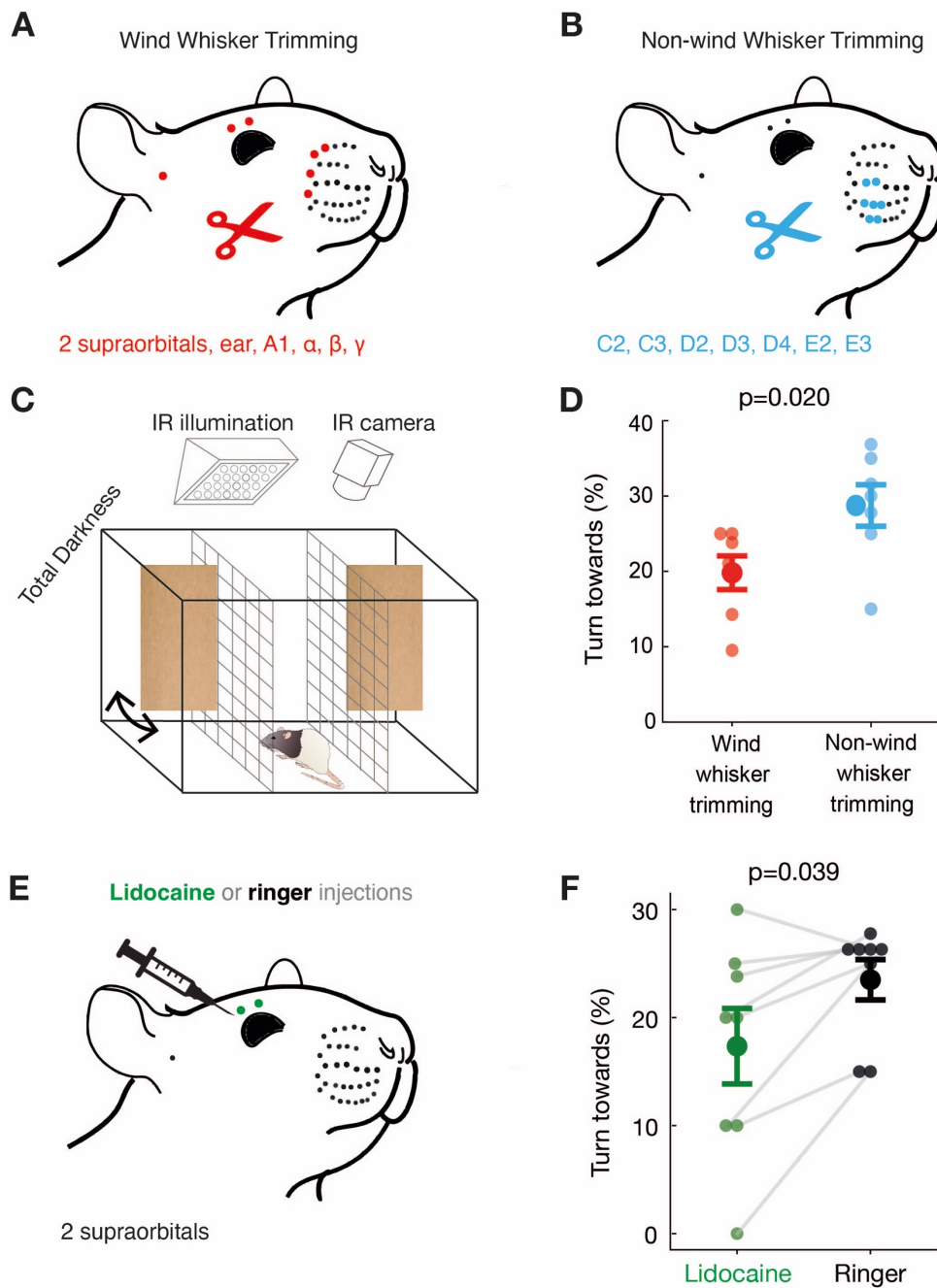
906
Figure 7. Differential effects of wind-whisker trimming and supraorbital nerve blockade on rat airflow turning responses

A, Wind-sensitive whiskers (2 supraorbital, ear, A1, α, β, γ whiskers) were trimmed bilaterally in 7 rats.

B, Wind-insensitive whiskers (C2, C3, D2, D3, D4, E2 and E3) were trimmed bilaterally in another 7 rats.

C, Cardboard-flaps were used to deliver wind stimuli in the turning-behavior arena, each trial being separated by 10 seconds and at randomized positions; see Figure 4*C*.

D, Wind-whisker-trimmed animals (red) turn towards flaps less strongly (p=0.039, unpaired Mann-Whitney-U-test, two-tailed, N=7 animals) than non-wind-whisker-trimmed animals (blue).

918   ***E,*** The supraorbital whisker follicles were targeted with lidocaine (green) or Ringer
919   solution (gray) in 8 individuals in a paired procedure.
920   ***F***, Lidocaine in supraorbital whiskers (green) significantly decreased airflow turning
921   responses relative to Ringer injection (p = 0.02; Wilcoxon signed-rank test, two-
922   tailed, N = 8 animals, 20 trials each).
923
924
925

926 **Supplementary Material**

927

928 **Movie 1.** Whisker movements in no (shielded) airflow conditions and low (ambient)
929 airflow conditions. Note the selective engagement of supraorbital whiskers in low
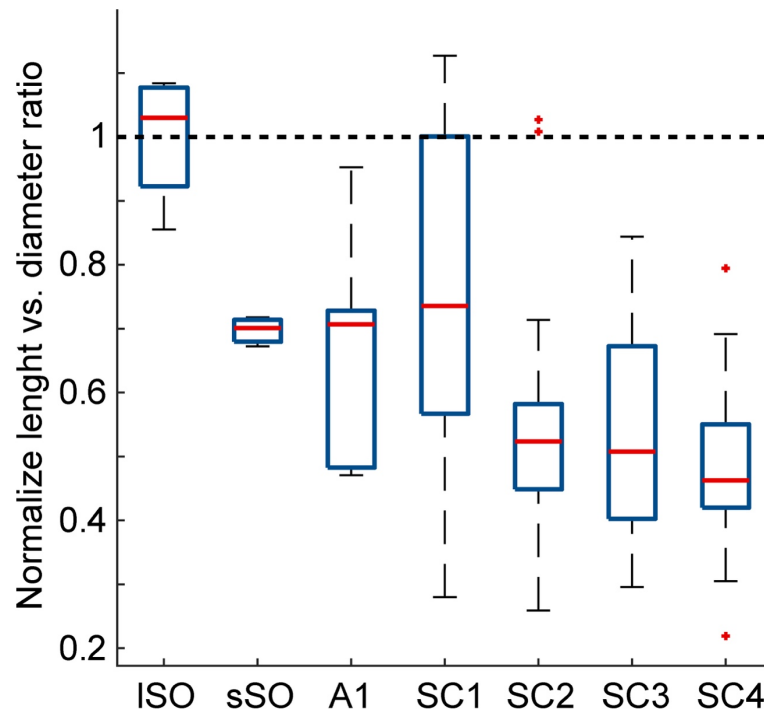930 airflow conditions.

931 https://figshare.com/s/f259cc52d7b7fae2976b

932

933 **Movie 2.** Airflow whisker responses recorded *ex vivo* with extracted whiskers.

934 https://figshare.com/s/9c9c2aca5f87ecab31b1

935

936
937

938
939 **Figure S1.**
940 *A*, Boxplot for the whisker length-diameter ratio normalized by the mean lSO ratio.
941 Ratios were arranged according to the semicircular configuration, which exhibited the
942 lowest observed p-value with respect to a shuffled distribution for that configuration
943 (semicircular, p-value = 0.018). See methods for a full list of p-values. Kruskal-Wallis
944 test, semicircular grouping as factor [H (6, 69) = 24.07, p = 0.0005]. Tuckey post hoc
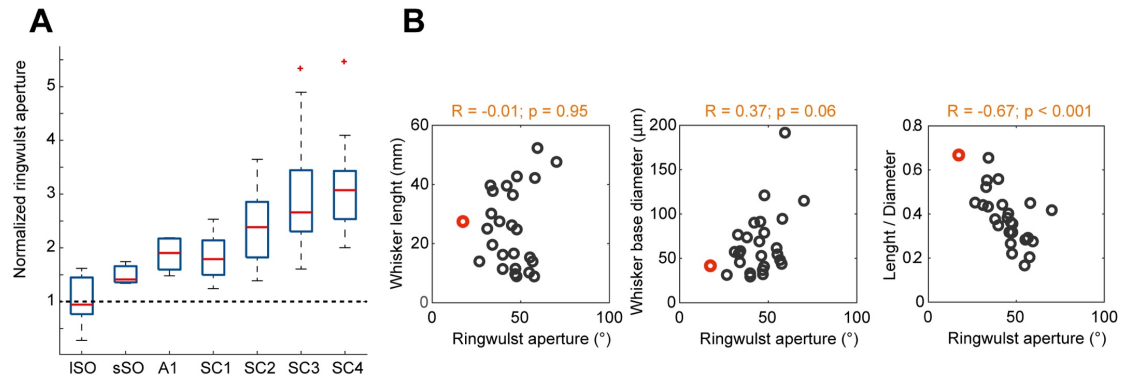945 indicated that groups SC2, 3 and 4 differed significantly from lSO (p < 0.04).
946 Additionally, group SC1 differed from SC4 (p = 0.001).
947
948

949
950

951
952

953 **Figure S2.**

954 *A,* Boxplot for the ring-wulst aperture normalized by the mean lSO aperture. Apertures
955 were arranged according to a semicircular configuration, which exhibited the lowest
956 observed p-value with respect to a shuffled distribution for that configuration
957 (semicircular, p-value < 0.0001). See methods for a full list of p-values. Kruskal-Wallis
958 test, semicircular grouping as factor [H (6, 122) = 61.69, p < 0.0001]. Tuckey post hoc
959 indicated that groups SC2, 3 and 4 differed significantly from lSO (ps < 0.02). In
960 addition, SSO and SC1 differed from SC3 and 4 (ps < 0.04) and A1 from SC4 (p =
961 0.02). Finally, SC2 differed from SC 4 (p = 0.03).

962 *B,* From left to right, Spearman correlations between: whisker length, whisker base
963 diameter and the ratio between them and ring-wulst aperture. Only the length-diameter
964 ratio was significantly correlated with ring-wulst aperture, indicative of an inverse
965 relation between the variables (R = -0.67; p < 0.001).

966
967
968
969
970